nature communications

Article

https://doi.org/10.1038/s41467-026-70052-8

Gear-like MOF microrobots for single cell mechanotransduction of microvilli

Received: 27 April 2025

Accepted: 17 February 2026

Published online: 26 February 2026

Check for updates

Xiaoxia Liu[1,2], Yong Wang[3] ✉, Lin Lin[4], Ning Liu[5], Zihao Yang[6], Peng Wang[1], Xiaohui Yan[4], Jinhong Guo[3,7], Dongdong Jin[1] ✉ & Xing Ma[1] ✉

Cellular mechanotransduction, mediated by specialized structures such as microvilli, regulates processes ranging from tissue homeostasis to disease progression. Existing tools for microvilli-specific biomechanical intervention suffer from limited spatiotemporal precision and non-physiological constraints, restricting mechanistic studies and targeted therapies. Here, we develop a magnetically driven gear-like metal-organic framework microrobot (MOFbot) for programmable mechanical manipulation of single-cell microvilli. MOFbots are fabricated through epitaxial growth of heterogeneous MOF structures followed by deposition of Ni/Au nanofilms. Under a rotating magnetic field, they perform rolling and obstacle negotiation. Their rotating gear structure entangles microvilli, exerting quantified pulling forces via Förster resonance energy transfer and traction force microscopy. This mechanical stimulation triggers intracellular calcium influx and enhanced focal adhesion kinase phosphorylation, indicating mechanotransduction pathway activation. Consequently, rotating MOFbots increase membrane permeability, enabling on-demand transmembrane delivery of therapeutics into targeted single cells. This work establishes a targeted cellular mechanomodulation strategy and informs future micro/nanorobotic biomedical designs.

Cells exist within dynamic mechanical microenvironments where external forces regulate essential processes through mechanotransduction pathways[1,2]. These mechanical stimuli are converted into biochemical signals via mechanosensitive ion channels (e.g., Piezo1, TRPV4)[3,4], cytoskeletal reorganization[5], and nuclear mechanotransduction mechanisms (e.g., YAP/TAZ signaling)[6,7], ultimately shaping tissue homeostasis and disease progression. Among cellular surface microstructures, microvilli emerge as force-transducing scaffold[8]. For instance, brush-border microvilli in renal proximal tubules convert hydrodynamic torque into cytoskeletal rearrangements to regulate ion transport[9], while immune cell microvilli probe antigen-presenting surfaces to initiate T-cell activation[10]. Quantitative studies reveal that fluid-induced torque at microvillar tips generates a ~40-fold mechanical amplification at cortical actin anchoring points[11], underscoring their role as biological force multipliers. Despite this significance, current tools still lack spatiotemporal precision to dissect their mechanotransduction dynamics. Developing methodologies for localized mechanical perturbation of microvilli is thus essential to unravel their mechanobiological contributions to tissue homeostasis and disease[12,13].

Bulk fluid shear stress has been used to study the effect of microvilli mechanics on cell mechanoresponses[14,15], while nanoscale

[1]Sauvage Laboratory for Smart Materials, School of Integrated Circuits, Harbin Institute of Technology (Shenzhen), Shenzhen, China. [2]School of Biomedical Engineering and Medical Imaging, Army Medical University, Chongqing, China. [3]Key Laboratory of Clinical Laboratory Diagnostics (Chinese Ministry of Education), College of Laboratory Medicine, Chongqing Medical University, Chongqing, China. [4]State Key Laboratory of Molecular Vaccinology and Molecular Diagnostics & Center for Molecular Imaging and Translational Medicine, School of Public Health, Xiamen University, Xiamen, China. [5]School of Aerospace Engineering and Applied Mechanics, Tongji University, Shanghai, China. [6]School of Computing and Artificial Intelligence, Southwest Jiaotong University, Chengdu, China. [7]School of Automation and Intelligent Sensing, Shanghai Jiao Tong University, Shanghai, China.
✉e-mail: wangyong@cqmu.edu.cn; jindongdong@hit.edu.cn; maxing@hit.edu.cn

geometric confinement (e.g., 200-nm nanopores) is capable of imposing non-specific mechanical constraints and altering mechanical signaling outcomes through artificial geometric restrictions, contributing to the enhancement of T-cell receptor clustering and activation[16]. Nevertheless, these methods cannot selectively target microvilli subpopulations or replicate physiological force dynamics. Recent advances in micro/nanorobotics offer transformative solutions through energy-converting actuators capable of drug delivery[17,18], microsurgery[19–21] and cell manipulation[22–24]. Among them, magnetic micro/nanorobots stand out due to their contactless manipulation capability, real-time controllability and inherent miniaturization[25,26], all of which are aligning with the demands of precision mechanobiology. Unlike substrate-based methods, untethered magnetic micro/nanorobots could deliver programmable mechanical stimuli to specific microvilli without physical confinement artifacts. However, no existing platform integrates targeted mechanical actuation, physiological compatibility, and multifunctional operation for microvilli mechanical modulation. Bridging this gap requires a miniature device capable of applying spatially resolved forces while maintaining native cellular microenvironments, a challenge central to advancing mechanotherapeutic innovation.

Herein, we present a magnetic gear-like MOFbot capable of targeted regulation of cellular mechanics through precise manipulation of microvilli substructures. The MOFbots featured with gear-like shape are constructed by epitaxial growth of heterogeneous MOF, and subsequently coated with Ni and Au layers. By applying a rotating magnetic field within different directions, two distinct motion modes of rolling and climbing can be achieved. Taking advantage of the gear-like structure, the MOFbots can effectively engage and entangle with microvilli on the cell membrane, enhancing its adhesion stability and mechanical interaction with living cells under magnetic field. Thus, the gear-like MOFbot can directly apply mechanical stimulation onto HeLa cells, leading to increased level of tractive force and intracellular calcium signaling. By remotely navigating the gear-like MOFbots to target single cancer cell and stimulate the microvilli mechanically, the membrane's permeability can be effectively altered, facilitating targeted intracellular delivery of anti-cancer drugs preloaded within the MOFbots' porous framework. Therefore, the multifunctional MOFbots demonstrate tremendous potential for programmable mechanical manipulation of cellular membrane mechanics and as well as targeted mechano/chemo-synergic therapy.

Results

Fabrication and characterization of magnetic gear-like MOFbot

We constructed a hybrid nanostructure by growing zinc-based MOF materials (ZIF-8) at the specific corner regions of a titanium-based MOF crystals (MIL-125), using a controlled method known as site-selective growth. This enabled the controlled formation of a heterogeneous MOF composite, MIL-125@ZIF-8, whose gear-like structural features are illustrated schematically in Fig. 1a. Afterwards, we deposited Ni and Au films onto the hybrid MOF composite using electron beam evaporation, resulting in a gear-like magnetic microrobot, termed a MOFbot. More specifically, the MIL-125 MOF with a tetragonal shape was first prepared using a solvothermal approach. Field-emission scanning electron microscopy (SEM) images (Fig. 1b) reveal the well-dispersed MIL-125 nanoparticles with a side length of approximately 1 µm. ZIF-8 MOF was then grown directly onto the four corners of MIL-125, resulting in the formation of MOF-on-MOF (MIL-125@ZIF-8) heterostructures. SEM and fluorescence images (Fig. 1c and Supplementary Fig. 1) of the synthesized MIL-125@ZIF-8 display a distinct and uniform gear-like morphology. The line scanning profile and elemental mapping (Supplementary Fig. 2) reveal that Zn element from ZIF-8 is concentrated at these corners, while Ti element from MIL-125 is located within the central core.

The Fourier transform infrared (FTIR) spectra (Fig. 1d) of MIL-125@ZIF-8 shows bands at 2903 cm^{-1}, 1262 cm^{-1}, and 1526 cm^{-1}, corresponding to the CH_3 group of 2-Methylimidazole in ZIF-8 and the carboxyl group of aminoterephthalate in MIL-125, respectively. The nitrogen (N_2) adsorption/desorption isotherms (Fig. 1e, Supplementary Fig. 3 and Supplementary Table 1) confirm the microporous nature of MIL-125@ZIF-8, and the specific surface area was identified to be 856.2 m^2/g, indicating its potential for drug loading applications. As shown in Fig. 1f, powder X-ray diffraction (XRD) analysis verified the high crystallinity of the prepared ZIF-8, MIL-125, and MIL125@ZIF-8. Furthermore, enlarged XRD patterns (Fig. 1g) demonstrate that the lattice parameters of the MIL-125 remain unchanged during the growth of ZIF-8. However, in comparison to the diffraction peaks of individual ZIF-8 and MIL-125, the peaks corresponding to the {110} and {002} crystal planes of ZIF-8 in MIL-125@ZIF-8 show slight right shifts, suggesting lattice modifications in ZIF-8 as it integrates with MIL-125[27].

To impart magnetism to the as-prepared MIL-125@ZIF-8, a 50 nm Ni layer was first deposited on its surface by electron beam evaporation, followed by a 10 nm Au layer to enhance biocompatibility. As shown in Fig. 1h, i, the resulting MIL-125@ZIF-8@Ni@Au structure retains the original gear-like morphology of MIL-125@ZIF-8. Elemental mapping confirms that the Ni and Au layers uniformly were coated on the surface, covering the entire structure and validating the successful fabrication of the magnetic gear-like MOFbot.

Controlled motion performance of magnetic gear-like MOFbot

The locomotion of the gear-like MOFbot was actuated by rotating magnetic fields generated by a custom-built magnetic field generator. This setup allowed for real-time and dynamic control over the magnetic field's strength, frequency and direction through modulation of the input current parameters, thereby enabling precise regulation of the MOFbot's motion, including its speed, direction, and trajectory. (Fig. 2a).

Under a horizontally applied rotating magnetic field, the MOFbot exhibited a distinct self-rotating behavior, as captured in the time-lapse images from Supplementary Movie 1 (Fig. 2b, upper row). The rotational dynamics were critically dependent on the frequency of the magnetic field at a fixed strength of 6 mT (Fig. 2c). At frequencies below a critical threshold of 7 Hz, the rotational rate of the MOFbot increased proportionally with the field frequency. In this regime, the magnetic torque applied to the MOFbot was sufficient to overcome the viscous resistance of the fluid medium. However, when the frequency exceeded this critical point (7 Hz), the rotational speed began to decline with further increases in field frequency. This phenomenon occurred because the available magnetic torque could no longer keep pace with the rapidly increasing fluid resistance, leading to asynchronous motion between the MOFbot and the driving field. This critical threshold, known as the step-out frequency, is a key performance parameter that is highly sensitive to the viscosity of the surrounding liquid.

In contrast, when subjected to a vertically rotating magnetic field, the MOFbot demonstrated efficient rolling and translational propulsion, as shown in Supplementary Movie 2 and the corresponding time-lapse images (Fig. 2b, lower row). Similar to the rotational behavior, the translational speed was a function of the external magnetic field frequency. It increased from 1.01 µm/s at 1 Hz to 6.45 µm/s at 6 Hz (Fig. 2d), showcasing controllable directional movement.

To gain insight into the underlying hydrodynamic interactions, COMSOL Multiphysics 6.1 simulations were employed to analyze the fluid velocity profiles and stress distributions on the surface of the rotating gear-like MOFbot. The simulations revealed that the flow velocity peaked at the four corners of the MOFbot, corresponding to the points of maximum linear velocity during rotation (Fig. 2e). Both the induced flow velocity and the associated stress on the MOFbot

https://doi.org/10.1038/s41467-026-70052-8

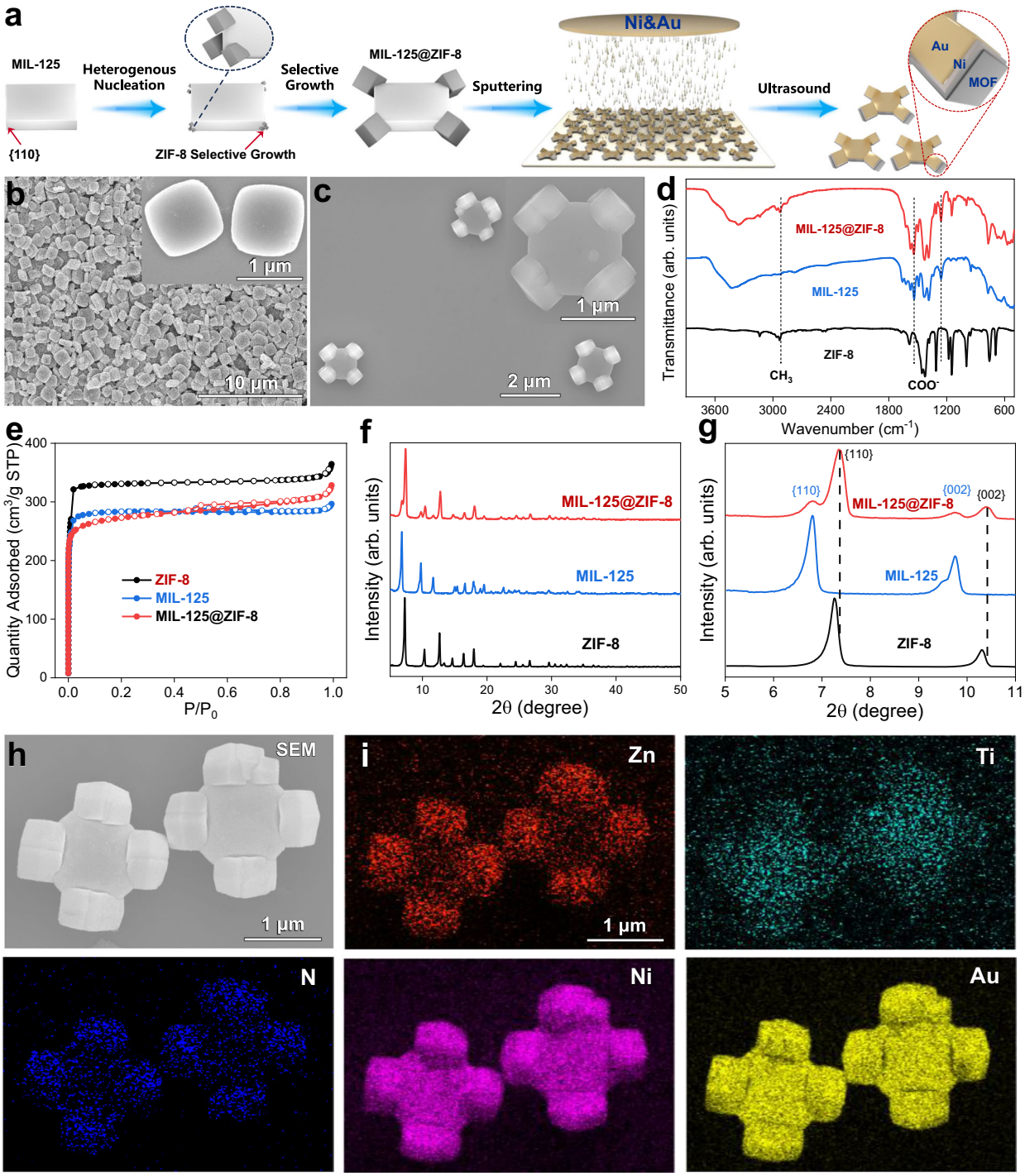

Fig. 1 | Fabrication and characterization of the gear-like MOFbots. a Schematic illustration of the preparation process for the gear-like MOFbots. SEM images of (**b**) MIL-125, (**c**) MIL-125@ZIF-8 particles. **d** FT-IR spectra of the as-prepared MIL-125, ZIF-8 and MIL-125@ZIF-8 microparticles. **e** N_2 absorption/desorption isotherms of the as-prepared MIL-125, ZIF-8, and MIL-125@ZIF-8 microparticles. P: the abbreviation of pressure. **f**, **g** Powder XRD patterns and the enlarged XRD patterns of the as-prepared MIL-125, ZIF-8 and MIL-125@ZIF-8 microparticles. **h**, **i** SEM image and EDX mapping of gear-like MOFbots. In (**b**, **c**, **h**), the experiments were repeated independently three times with similar results, and a representative result is shown for each.

surface were influenced by the magnetic field parameters, reaching maximum values of approximately 46 μm/s and 0.55 Pa, respectively, at the critical frequency of 7 Hz (Fig. 2f, Supplementary Fig. 4). The concentration of stress at the corners and the optimal hydrodynamic output at this step-out frequency establish a functional threshold for biomedical applications. The maximized shear forces and pressure generated at 7 Hz are particularly relevant for potential applications such as regulating cell membrane permeability or triggering mechanosensitive signaling pathways in drug delivery and cellular mechanotransduction.

Furthermore, to evaluate the locomotion performance of the gear-like MOFbot on complex surfaces, microtopographical patterns with a constant cross-sectional profile were fabricated using a laser direct writing (LDW) system (Fig. 2g–i). A platform with a height of 1.5 μm and a 90° inclination angle served as a barrier to test climbing capability. As demonstrated in Fig. 2j and Supplementary Movie 3,

https://doi.org/10.1038/s41467-026-70052-8

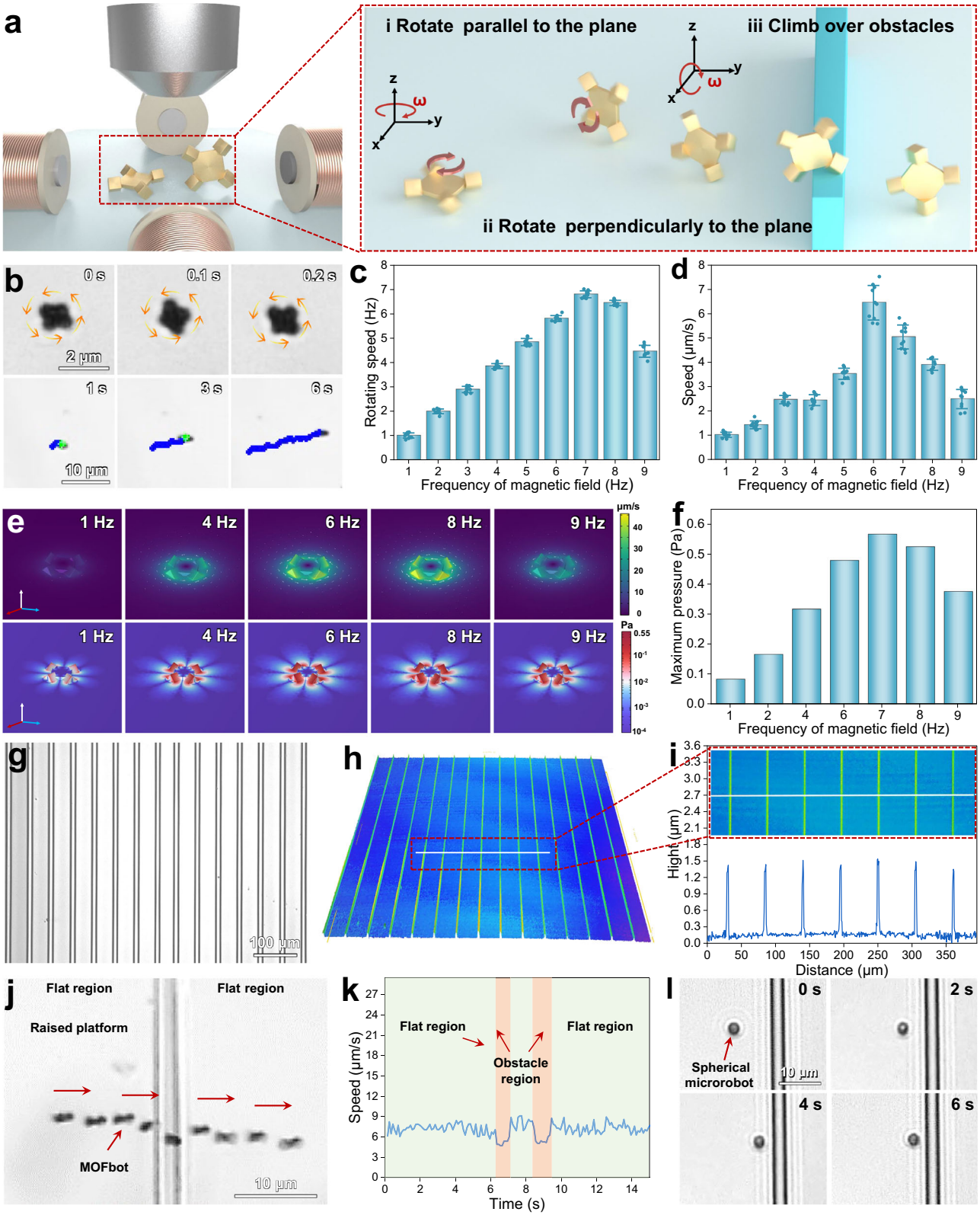

Fig. 2 | Magnetically controlled motion behaviors of the gear-like MOFbot. **a** Schematic illustration of microrobot motion manipulation by the horizontally and vertically rotating magnetic fields. **b** Rotating and rolling motion of gear-like MOFbot at different time intervals. The frequency of horizontally and vertically rotating magnetic fields are 7 and 6 Hz, respectively. **c**, **d** Average rotational rate and translational velocity of the gear-like MOFbot under the actuation of magnetic field (6 mT) at different frequencies ($N = 10$ independent samples). **e** Simulation of the flow field and fluid pressure distribution induced by the rotation of gear-like MOFbot with different frequencies. **f** Quantitative analysis of the maximum fluid pressure induced by the rotation of gear-like MOFbot with different frequencies. **g**–**i** Optical images and surface topography of the patterned substrate using a 3D surface profiler. **j** Superimposed image of the sequential frames of a gear-like MOFbot overcoming obstacles on the patterned substrate. **k** The instantaneous velocity of gear-like MOFbot when moving across the patterned substrate. **l** Time-lapse images of a moving PS@Ni@Au spherical microrobot on the patterned substrate. Data in (**c**, **d**) are the mean ± S.D.

under the actuation of a vertically rotating magnetic field (6 mT, 6 Hz), the gear-like MOFbot successfully navigated the three-dimensional structured surface and overcame the vertical obstacle via a "climbing-stairs" effect. The instantaneous speed recorded during this maneuver reached a maximum of approximately 9 μm/s (Fig. 2k). In a control experiment, spherical microrobot (i.e., PS@Ni@Au fabricated by depositing Ni and Au layers on polystyrene microspheres) failed to traverse the same obstacles (Fig. 2l, Supplementary Fig. 5-6, Supplementary Movie 4). This comparative result underscores that the unique gear-like morphology significantly enhances the motion adaptability and terrain negotiation capabilities of the MOFbot, which is crucial for practical applications in complex biological environments.

Interaction between the magnetic gear-like MOFbot and cell microvilli

The cell membrane features intricate structures, among which microvilli stand out as actin-based membrane protrusions with versatile functions, including nutrient absorption, secretion, and mechanotransduction. Confocal laser scanning microscope (CLSM) and SEM images have revealed an abundance of microvilli on the surface of HeLa cells (Supplementary Fig. 7). We labeled the gear-like MOFbots with the green fluorescent dye (FITC) and then observed the interaction between the gear-like MOFbots and cellular microvilli using CLSM. As shown in Fig. 3a and Supplementary Movie 5, the green fluorescent gear-like MOFbots were embedded within the red fluorescent cellular microvilli. Additionally, in the 3D view of CLSM, the green fluorescent MOFbots appear yellow due to their colocalization with the red fluorescent microvilli on the cell membrane. SEM image also clearly shows that the gear-like MOFbots were intertwined with the microvilli, residing within their internal structure (Fig. 3a). These results confirm that, under a magnetic field, the gear-like MOFbots exerted significant mechanical interactions with the microvilli on the cell membrane, including pulling and intertwining.

In contrast, under static conditions with no applied magnetic field, the MOFbots remained passively adhered to the cell surface and showed no observable entanglement with microvilli (Fig. 3b). To directly test the role of morphology in microvilli entanglement, we performed shape-control experiments using spherical microrobots fabricated by coating polystyrene microspheres with sequential layers of Ni and Au. Although these spherical microrobots exhibited continuous rotation when subjected to the same magnetic actuation, both CLSM and SEM images confirmed their inability to entangle with microvilli (Fig. 3c). In both experimental scenarios including absence of motion or non-geared morphology, the microrobots predominantly reside on the surface of the microvilli, with minimal evidence of intertwining or deep interaction. The differences from the dynamically rotating gear-like MOFbots demonstrates that both magnetic field-driven motion and gear morphology are essential for achieving biologically significant mechanical coupling with cellular structures.

To quantitatively analyze the distribution of gear-like MOFbots within cellular microvilli, the Unet++ network model (Fig. 3d) was employed for semantic segmentation of 2D slices (z-stacks) from 3D confocal image volumes. This enables precise extraction of target cell regions and voxel-level identification, distinguishing cell structures from background. Following segmentation, feature parameters, namely saturation, color gamut, and brightness, were quantified across the entire 3D volume at the voxel level. This enabled voxel-wise classification, including discrimination between red and green staining signals, as well as normalized statistical evaluation of their spatial distribution. The details about the Unet++ network model are provided in Supplementary Information. This results further demonstrate that the gear-like MOFbots, owing to their distinctive structure and autonomous properties, engage in mechanical interactions with the microvilli, facilitating deep penetration and interfacial coupling within the cellular microvilli network (Fig. 3e–g and Supplementary Fig. 8). This dynamic interaction enables precise spatiotemporal control over mechanical stimuli directly applied onto the cell.

Analysis of mechanical stimulation on microvilli via magnetic gear-like MOFbot

Cells utilize traction forces to sense mechanical cues in their environment. As shown in Fig. 4a, the physical characteristics of the traction forces exerted by the magnetic gear-like MOFbot on the microvilli of HeLa cells were quantified using traction force microscopy (TFM). In this approach, HeLa cells were cultured on polyacrylamide (PA) gels embedded with fluorescent beads as tracking markers. The lateral deformation changes of the PA gels can be accurately tracked and measured as a reflection of the traction forces applied by the magnetic gear-like MOFbot onto the HeLa cells. We performed the imaging of cells before and after treatment with the magnetic gear-like MOFbot. The displacement of fluorescent beads and the traction stress exerted by cells in response to the magnetic gear-like MOFbot, both in the absence and presence of a magnetic field, were calculated using TFM, as described in previous studies[28]. As shown in Fig. 4b, c, when the gear-like MOFbots remain stationary, the fluorescent beads embedded within the PA gels exhibit minimal displacement, measuring approximately 0.12 μm. However, when the gear-like MOFbots rotate on the cell's surface and engages with the microvilli, the displacement of the fluorescent beads dramatically increases to approximately 0.88 μm, correlating with mechanical engagement of cellular microvilli. Corresponding traction stress maps (Fig. 4b, d) further demonstrated that rotating MOFbots induce localized mechanical stresses averaging 1.5 kPa via microvilli entanglement, a magnitude 15-fold greater than stationary controls (~0.1 kPa). This mechanical disparity directly confirms that the rotational motion of the gear-like MOFbots generates significant traction forces at the interface between the cell and the MOFbots.

To verify the role of cellular microvilli in force transduction, we performed siRNA-mediated knockdown of ezrin, which is a key scaffolding protein essential for microvilli integrity. Transient transfection of HeLa cells with ezrin-specific siRNA led to efficient suppression of ezrin expression, which in turn induced pronounced destabilization of microvillar protrusions. As a consequence, ezrin-depleted cells exhibited a substantial reduction in microvilli density. This morphological impairment was corroborated by both SEM and CLSM analyses, which consistently demonstrated a marked loss of surface microvilli relative to control cells (Supplementary Fig. 9). Under identical MOFbots stimulation, these microvilli-deficient HeLa cells exhibited significantly attenuated bead displacement and traction stress (Fig. 4b–d). These results demonstrate that mechanical forces are transmitted via microvilli to the underlying substrate, confirming the essential role of microvilli in mediating the physical interactions between MOFbots and cellular structures.

In addition, an actin tension probe based on Förster resonance energy transfer (FRET) technology[29] was employed to detect intracellular forces exerted by both stationary and rotating gear-like MOFbots. As illustrated in Fig. 4e, the probe consists of a dipole orientation-based FRET sensor positioned between β-actin monomers. This design enables real-time visualization of mechanical perturbations transmitted through the actin cytoskeleton. Under mechanical loading, the relative orientation of the donor-acceptor dipole pair is rotated from an approximately parallel alignment toward a more diagonal configuration, resulting in a characteristic decrease in FRET efficiency. This geometric transition provides a sensitive readout of forces acting on the actin filaments. To quantitatively evaluate the mechanical influence of gear-like MOFbots on HeLa cells, we monitored temporal changes in FRET efficiency under controlled magnetic actuation. Progressive extension of the magnetic field switching duration produced a monotonic decline in FRET efficiency, indicating a significant

https://doi.org/10.1038/s41467-026-70052-8

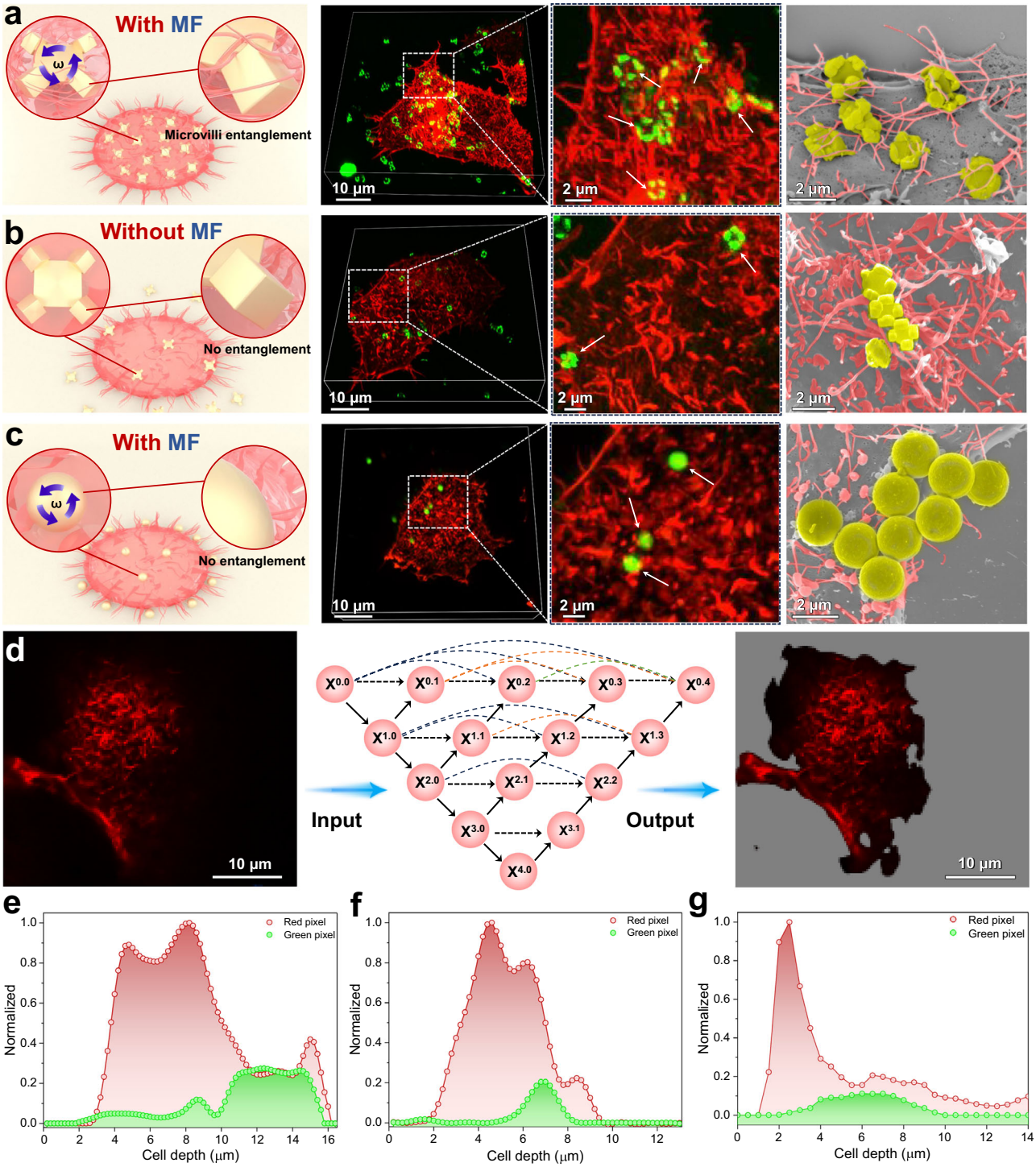

Fig. 3 | Interaction between cell microvilli and gear-like MOFbots. Representative CLSM views and SEM images illustrating the distribution of MOFbots on HeLa cells. **a** Gear-like MOFbots under external magnetic field actuation. **b** Gear-like MOFbots in the absence of magnetic field. **c** Spherical microrobots under external magnetic field actuation. MF: the abbreviation of magnetic field. In pseudo-colored SEM images, microrobots and microvilli were marked with yellow and red colors, respectively. **d** The U-Net + + network model used for semantic segmentation of cellular images, enabling precise extraction of target cell regions and voxel-level identification, effectively distinguishing cells from background. Each experiment was repeated independently for 3 times with similar results. Segmentation results from 3D reconstructions illustrating the distribution of each voxel type (red and green) in stained cells treated under different conditions: (**e**) gear-like MOFbots with a magnetic field, (**f**) gear-like MOFbots without a magnetic field, and (**g**) Spherical microrobots with a magnetic field.

mechanical interaction between the gear-like MOFbots and the cells under magnetic influence. Upon cessation of the magnetic field, FRET signals gradually returned to baseline, demonstrating the reversibility of the mechanical perturbation and the dissipation of MOFbot-induced forces (Fig. 4f, h and Supplementary Movie 6). Statistical analysis further confirmed the mechanical contribution of MOFbot rotation. Cells exposed to rotating gear-like MOFbots exhibited significantly lower FRET efficiencies, which correspond to higher intracellular traction forces, compared with cells incubated with stationary counterparts (Fig. 4i). These results collectively demonstrate that the

https://doi.org/10.1038/s41467-026-70052-8

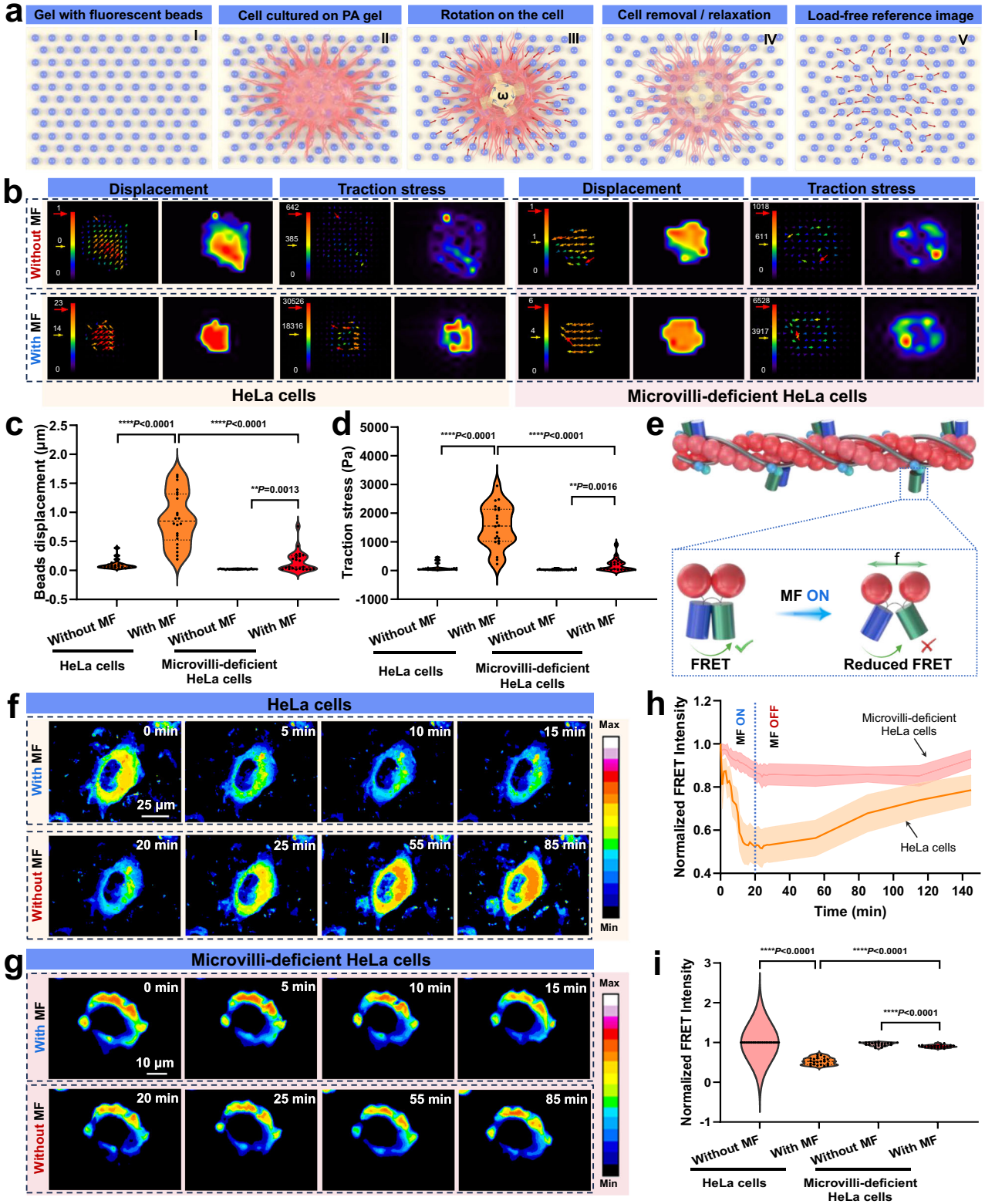

Fig. 4 | Analysis of mechanical forces generated by the gear-like MOFbots on cell through microvilli. a Schematic illustration of the traction force microscopy method. In this approach, cells are cultured on a PA gel substrate. Fluorescent beads are embedded on the surface of the PA gel to precisely track and quantify lateral deformations caused by cellular forces. **b** Representative displacement and traction stress maps of MOFbot-induced substrate deformation in normal and microvilli-deficient HeLa cells (without/with the actuation of magnetic field), derived from PA-induced lateral deformation. **c**, **d** Quantitative analysis of displacement and traction stress ($N = 22$ cells). Statistical differences were calculated using two-tailed Student's t test, $^{**}P < 0.01$, $^{****}P < 0.0001$. **e** Schematic illustration of the FRET-based actin force probe. **f**, **g** Representative time-lapse images displaying the change of FRET signals in normal and microvilli-deficient HeLa cells under the influence of MOFbots. **h** Quantitative analysis of the FRET signal intensity changes in different HeLa cells over time, shaded areas represent SD for $N = 22$ cells. **i** Average FRET signal in normal and microvilli-deficient HeLa cells at the initial time point without magnetic field (0 min) and after 15 min with magnetic field application (15 min) ($N = 22$ cells). MF magnetic field, FRET Förster resonance energy transfer. Statistical differences were calculated using two-tailed Student's t test, $^{****}P < 0.0001$.

rotational dynamics and gear-like architecture of MOFbots enable effective transmission of mechanical cues into the actin cytoskeleton, thereby eliciting measurable intracellular force responses. Critically, in control experiments performed under identical conditions without magnetic fields, the FRET efficiency in HeLa cells remained stable over time (Supplementary Fig. 10), effectively excluding contributions from spontaneous cellular deformation or photobleaching.

In addition, FRET efficiency measurements in microvilli-deficient HeLa cells revealed markedly reduced molecular tension and a lack of response to MOFbot-induced mechanical stimulation, further corroborating that the disruption of microvilli leads to a significant decrease in cellular traction forces and abolishes the cells' ability to transduce mechanical cues (Fig. 4g–i). These findings are consistent with the cell traction force measurements, reinforcing the critical role of microvilli in mediating cellular mechanotransduction. Moreover, treatment of HeLa cells with cytochalasin D, which is a known actin-disrupting agent, also induced microvilli collapse and cytoskeletal disorganization (Supplementary Fig. 11). Under these conditions, both TFM and FRET measurements showed nearly complete abrogation of MOFbot-induced traction forces and intracellular force responses (Supplementary Figs. 12, 13). These results demonstrate that an intact actin cytoskeleton including microvilli is indispensable for the force transmission elicited by MOFbot stimulation. These complementary lines of evidence confirm the essential role of microvilli in mediating the physical interactions between MOFbots and cellular structures. Overall, the rotational movement of the gear-like MOFbots interacting with the cell microvilli generated a significant mechanical effect on the cells. This dynamic interaction not only induced considerable traction forces but also influenced the mechanical properties of the cell membrane, indicating that the MOFbots can actively modulate cellular behavior. These findings underscore the potential of gear-like MOFbots as miniaturized artificial tool for manipulating cellular mechanics.

To further investigate the mechanical impact of rotating MOFbots on cellular microvilli, we developed a three-dimensional solid mechanics model in COMSOL Multiphysics 6.1. In the model, each microvillus was idealized as a 2 μm-long, 100 nm-diameter cylinder fixed to the surface of a hemispherical cell and assigned hyperelastic material properties, while the MOFbot was treated as a rigid body due to its higher structural stiffness (Supplementary Fig. 14). The MOFbot was set to rotate at 6.8 r/s, producing transient contact along its rotational trajectory. Contact interactions were simulated using a penalty-based contact mechanics approach, capturing microvillus bending, lateral deflection, and strain distribution. Geometric nonlinearity was included to ensure numerical stability under large deformations. Simulation results reveal pronounced lateral bending of the microvillus upon MOFbot contact, with traction concentrated from the proximal to middle regions, consistent with forced-bending morphology (Supplementary Fig. 15a). Surface integration of traction magnitudes estimated a maximum contact force of ~46 pN (Supplementary Fig. 15b), which emerges naturally from the MOFbot's rotational kinematics (tangential velocity ~4.3×10^{-5}m/s). These results corroborate experimental observations, indicating that MOFbot rotation can locally perturb microvilli, inducing deformation and intracellular force transmission.

Influence of the mechanical stimulation on calcium influx and phosphorylation levels of focal adhesion kinase (FAK)

Since mechanotransduction is closely linked to changes in calcium ion influx, the effects of magnetically induced mechanical forces on cells can be effectively monitored through fluorescence changes in the highly sensitive Ca^{2+} indicator (pCMV-jGCaMP7s) (Fig. 5a). To investigate the contribution of specific mechanosensitive channels to MOFbot-triggered Ca^{2+} influx, we pharmacologically inhibited PIEZO1 and TRPV4, which are two mechanoreceptors implicated in distinct force-sensing regimes. PIEZO1 generates rapid mechano-activated cation currents, while TRPV4 confers sensitivity to piconewton-scale forces. HeLa cells were pretreated with GsMTx4 (PIEZO1 inhibitor) and HC-067047 (TRPV4-specific antagonist). Time-lapse images of representative untreated control cell (Supplementary Movie 7, Fig. 5b) under MOFbot stimulation revealed a progressive increase in jGCaMP7s fluorescence intensity over time, corresponding directly to elevated cytosolic Ca^{2+} levels and thus demonstrating active calcium influx in response to mechanical force. Quantitative analysis confirmed that, in untreated control cells, the mean Ca^{2+} fluorescence intensity at $t = 480$ s was approximately twice that at baseline ($t = 0$ s) (Fig. 5c). In contrast, cells pre-incubated with either inhibitor exhibited markedly attenuated Ca^{2+} responses, with only negligible changes in fluorescence intensity over the same period. To assess population-level behavior, Ca^{2+} influx heat maps were generated for 50 cells under each of three conditions: untreated control, GsMTx4-treated, and HC-067047-treated (Fig. 5d–f). Each horizontal line represents the time-dependent intracellular Ca^{2+} change in an individual cell. In control cells, despite the cell-to-cell variation of calcium response, the majority of cells exhibited a significant increase in cytosolic Ca^{2+} concentration following mechanical stimulation (Fig. 5d). Conversely, more than 90% of cells pretreated with either inhibitor displayed suppressed Ca^{2+} signals, with minimal fluorescence elevation over time (Fig. 5e, f). Collectively, these results demonstrate that gear-like MOFbots elicit a robust intracellular calcium response, and that both PIEZO1 and TRPV4 channels are essential for efficient Ca^{2+} entry upon MOFbot-mediated mechanical stimulation.

To further elucidate the spatial redistribution of the mechanosensitive channels in response to force, we performed immunofluorescence staining for PIEZO1 and TRPV4 following MOFbot stimulation. HeLa cells incubated with MOFbots were exposed to a rotating magnetic field to apply localized mechanical force, with parallel control samples maintained without magnetic actuation to isolate the effect of the force itself. After fixation, cells were immunostained for PIEZO1 and TRPV4, with microvilli stained using phalloidin and nuclei labeled with DAPI. CLSM imaging revealed a force-dependent redistribution of both channels. In the absence of magnetic actuation, PIEZO1 and TRPV4 signals were diffuse along the plasma membrane (Supplementary Fig. 16a and Supplementary Fig. 17a). In contrast, upon MOFbot actuation, both channels exhibited pronounced translocation and concentrated localization to microvilli structures (Supplementary Figs. 16b, 17b). This enhanced co-localization with microvilli under mechanical stimulation indicates an active recruitment process, aligning with their functional role in microvilli-mediated mechanotransduction.

FAK undergoes autophosphorylation at tyrosine 397 in response to cytoskeletal contraction, thereby transmitting mechanical stimuli to a range of downstream signaling cascades[30]. We analyzed the phosphorylation levels of FAK at tyrosine 397 (pFAK) in HeLa cells treated with rotating gear-like MOFbots using immunofluorescence techniques. As shown in Fig. 5g, h, pFAK levels in HeLa cells were significantly elevated due to the mechanical forces exerted by the gear-like MOFbots. These findings suggest that the motion of the MOFbots indeed induced significant intracellular tension, which could further potentially deform the membrane structure of the cell.

Single cell targeted intracellular drug delivery by gear-like MOFbots

Having established that MOFbot-mediated mechanical forces on microvilli activate mechanotransduction pathways (e.g., Ca^{2+} signaling and FAK phosphorylation), we next investigated whether such mechanical perturbations could directly regulate the physical properties of the plasma membrane. Previous studies suggest that localized mechanical stress can induce lipid bilayer fluidization and transient pore formation, thereby enhancing membrane permeability[31,32]. As a proof-of-concept therapeutic application, we maneuvered the

https://doi.org/10.1038/s41467-026-70052-8

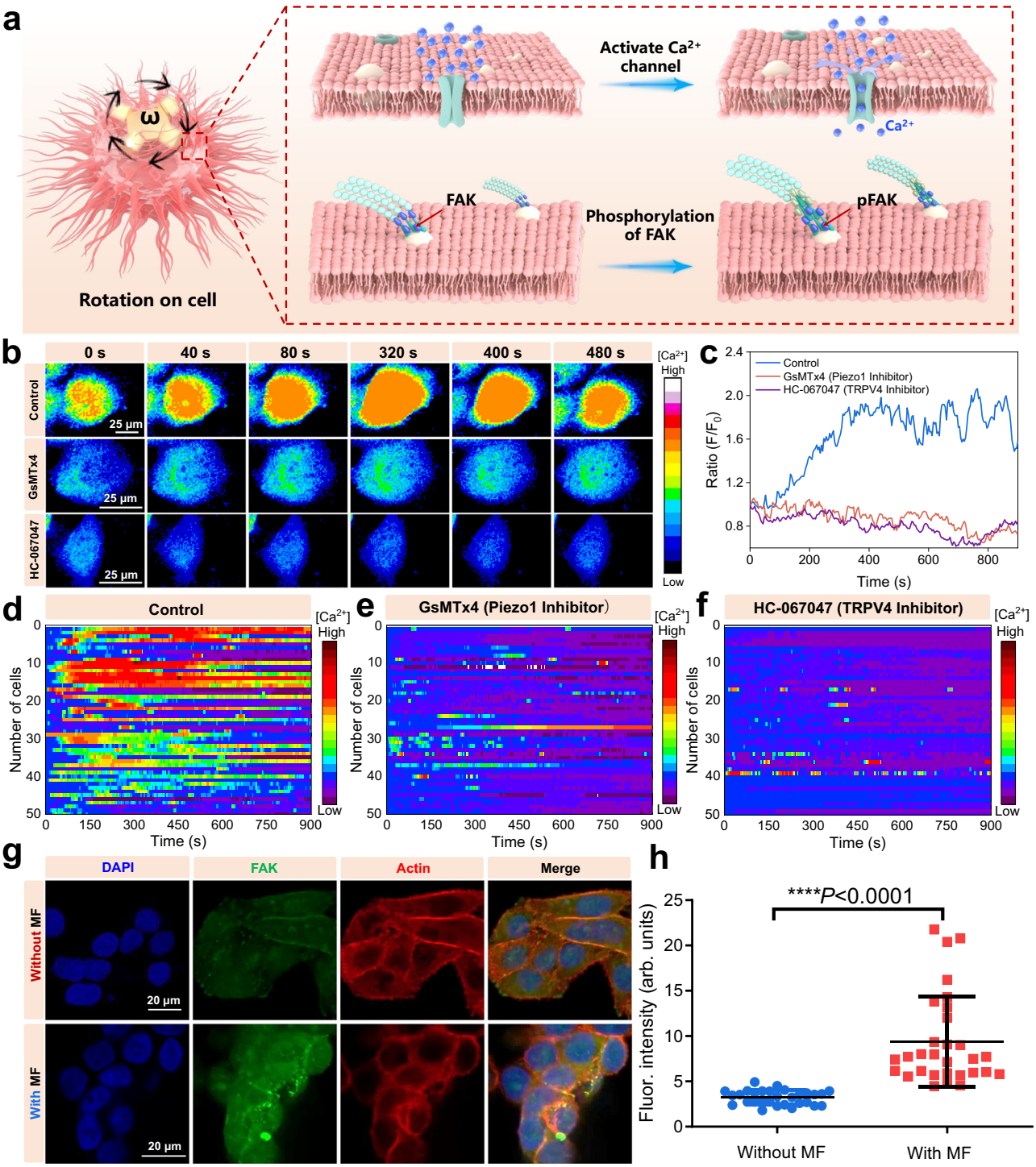

Fig. 5 | The levels of Ca^{2+} influx and phosphorylated FAK (pFAK) in HeLa cells induced by the mechanical forces exerted by the gear-like MOFbots. **a** Schematic illustration showing that the active motion of the gear-like MOFbots induces the Ca^{2+} influx and phosphorylation of FAK. **b**, **c** Fluorescence images and normalized fluorescence intensity of intracellular Ca^{2+} in response to gear-like MOFbot treatment under three conditions: untreated control cells, cells pre-incubated with 1 μM GsMTx4 (Piezo1 inhibitor), and cells pre-incubated with HC-067047 (TRPV4 antagonist, 1 μM). In Fig. 5b, the experiments were repeated independently three times with similar results, and a representative result is shown for each. *F* the abbreviation of fluorescence. **d**–**f** Color-scaled heat map depicting the Ca^{2+} response in HeLa cells under three conditions: untreated control, cells incubated with Piezo1 inhibitor GsMTx4, and cells incubated with TRPV4 antagonist HC-067047, upon treatment with gear-like MOFbots ($N = 50$ cells). **g**, **h** Representative fluorescence images and average intensities of pFAK in HeLa cells exposed to the gear-like MOFbots, analyzed under conditions with and without the application of a magnetic field. In Fig. 5g, MF: the abbreviation of magnetic field, the experiments were repeated independently three times with similar results, and a representative result is shown for each. All values represent the mean ± SD for $N = 50$ cells. Statistical differences were calculated using two-tailed Student's t test, $^{****}P < 0.0001$.

magnetic gear-like MOFbot to approach a targeted cell, climbing onto the cell surface to interact with the cellular microvilli, then utilized the mechanical forces exerted by the MOFbots to enhance the transmembrane delivery of loaded substances into the targeted cell (Fig. 6a). Firstly, the biomechanical transformations were theoretically validated through coarse-grained molecular dynamics (CGMD) simulations (Fig. 6b and Supplementary Fig. 18). As time prolonged, magnetic field-driven rotation of MOFbots induced progressive disordering of phospholipid packing at microvilli interfaces. The phenomenon not only confirms programmable mechanotransduction at cellular interfaces but also introduces a magnetically controllable strategy for efficient transmembrane cargo delivery. Subsequently, a typical experiment demonstrating the locomotion of a gear-like MOFbot as it moves toward, climbs onto and rotates on a cell is shown in Supplementary Movie 8. The corresponding optical images and the plot of instantaneous velocity *versus* time are shown in Fig. 6c, d. The whole process is divided into three stages as follows. i) Targeting the cell: in the initial stage, under the influence of the vertical

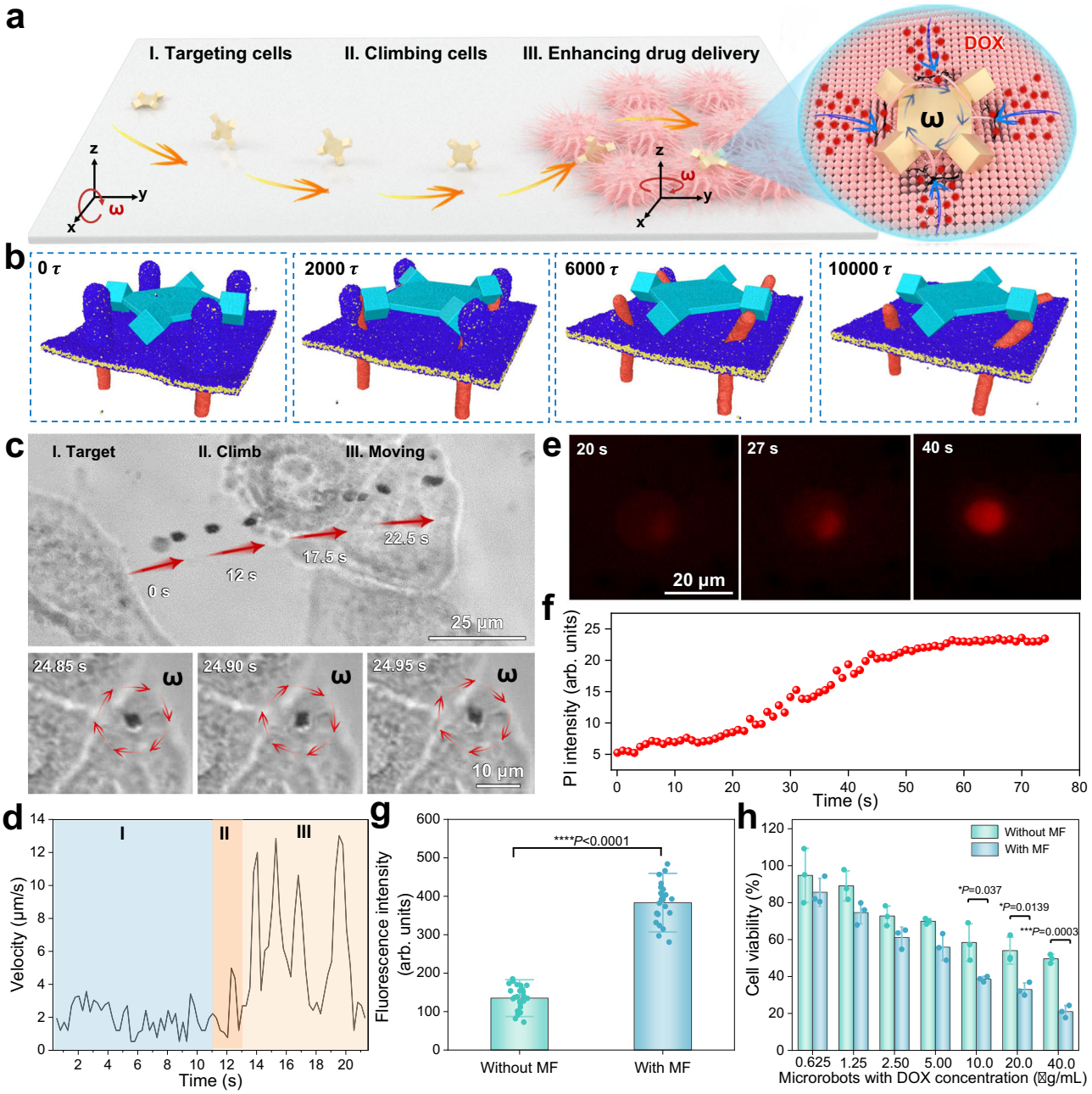

Fig. 6 | Mechanical stimulation induced change of membrane permeability and enhanced intracellular drug delivery by the gear-like MOFbots. a Schematic illustration depicting the active targeting of a cell and active motion enabled regulation of membrane permeabilization for transmembrane delivery. **b** Simulation result of the interaction between the gear-like MOFbot and cellular microvilli. **c**, **d** Superimposed images of sequential frames and instantaneous velocity illustrating the targeting, approaching, and interaction processes between the HeLa cell and the gear-like MOFbot. **e**, **f** Time-lapse fluorescence images and corresponding intensity analysis depicting the dynamic intracellular distribution of PI following treatment with gear-like MOFbots. PI: the abbreviation of propidium iodide. **g** The average fluorescence intensities of DOX in HeLa cells exposed to the gear-like MOFbots under conditions with and without the application of a magnetic field ($N = 25$ cells). MF: the abbreviation of magnetic field. Statistical differences were calculated using two-tailed Student's t test, $^{****}P < 0.0001$. **h** Viability of HeLa cells treated with the different concentrations of DOX-loaded gear-like MOFbots ($N = 3$ independent samples). Statistical differences were calculated using two-tailed Student's t test, $^{*}P < 0.05$,$^{***}P < 0.001$. Data in g and h are the mean ± S.D.

rotating magnetic field, the gear-like MOFbot approaches the target cell at an average speed of 3.5 μm/s. ii) Contacting and climbing onto the cell surface: at t = 12 s, the MOFbot makes contact with the cell. Driven by the magnetic field, it then climbs onto the cell surface. iii) Linear movement on the cell surface: at t = 14 s, the MOFbot moves across the cell surface at an average speed of 9 μm/s. Though velocity fluctuations were observed, a phenomenon similar to that recently reported with microparticles propelled on surfaces with microtopographies[33], an enhanced translational velocity was noted when moving on the cell surface. In our experiment, the adherent cells generated a surface topography that increased friction, thereby facilitating the rolling motion of the MOFbot and resulting in similar observations. At t = 24 s, the magnetic field direction is switched to the x-y axis, prompting the MOFbot to rotate on the cell surface and engage with the cell's microvilli.

To investigate the effect of mechanical stimulation exerted by the gear-like MOFbot on cell membrane permeability, propidium iodide (PI) is selected as a model drug molecule. PI is a red fluorescent dye that cannot cross the intact membrane of live cells, making it an ideal probe for studying transmembrane transport. Thus, by using PI, we can directly observe how the mechanical action of the MOFbots influences the permeability of the cell membrane. As shown in Fig. 6e, f and Supplementary Movie 9, upon rotation of the gear-like MOFbot on the cell surface, PI fluorescence first appears in the cell nucleus. Over time, the intensity of the red fluorescence in the nucleus progressively increases. By 60 s, the fluorescence inside the cell stabilizes. This result confirms that the MOFbot's rotational movement likely alters the cell membrane's permeability, allowing PI to enter the intracellular environment to bind with DNA in the nucleus. Both CLSM and flow cytometry results consistently show that the PI fluorescence intensity in cells with magnetic field activation is more than 8 times higher than the static control group (Supplementary Figs. 19, 20). To exclude the possibility that increased cell membrane permeability is due to cell death, cell viability is assessed using the CCK-8 assay after treatment with the gear-like MOFbots. As shown in Supplementary Fig. 21, under both magnetic and non-magnetic field conditions, the cell viability remained above 90%, even at a MOFbot concentration of 320 μg/mL. This indicates that the motion of the MOFbots has negligible impact on cell viability within the time period under study. These findings confirm that the gear-like MOFbot effectively enhances the permeability of the cell membrane.

Due to its porous structure, the gear-like MOFbot is highly efficient in adsorbing and carrying a wide range of small molecules. As a result, we successfully loaded the anticancer drug doxorubicin (DOX) into the MOFbot's nanopores, achieving a drug loading capacity of approximately 321 μg/mg (Supplementary Figs. 22, 23). We investigated the impact of the autonomous movement of gear-like MOFbots on the release behavior of DOX in vitro. The results revealed a significant increase in DOX release when the MOFbots were rotated by a magnetic field, as compared to the group without magnetic field, which indicates that the autonomous motion of the gear-like MOFbots could accelerate DOX release (Supplementary Fig. 24), providing feasibility of remotely controlled drug release at targeted site. Subsequently, we then assessed the effect of the MOFbot's motion on DOX uptake by the cells. As shown in Fig. 6g and Supplementary Fig. 25, the DOX fluorescence intensity inside cells treated with magnetic-field-driven gear-like MOFbots is approximately 2.8 times higher than in cells treated with stationary MOFbots. Moreover, at the same concentration of MOFbots, cell viability in the rotating MOFbot group under the magnetic field is consistently lower than that in the control group, which is treated with stationary MOFbots (Fig. 6h). Take together, these results provide clear evidence that the motion of the gear-like MOFbots significantly enhances transmembrane drug delivery. Meanwhile, the successful internalization of cargo molecules serves as a functional readout of microrobot-generated mechanostimulation. The observed changes in cell membrane permeability can be attributed to two main factors: First, the gear-like MOFbot, driven by magnetic forces under the influence of the magnetic field, interacts with the microvilli on the cell surface. This interaction based on mechanical forces may stretch and deform the microvilli, leading to structural alterations in the cell membrane. These changes in membrane structure likely affect its flexibility and elasticity, thereby influencing its permeability[5,34]. Furthermore, the plasma membrane plays a key role in cellular mechanical responses via mechanosensitive ion channels. These channels, typically proteins embedded in the cell membrane, undergo conformational changes in response to local forces. Such forces can arise from increased membrane tension, alterations in membrane curvature, or mechanical forces exerted by the cytoskeletal network and/or the extracellular matrix on the channels[35,36]. Therefore, the mechanical movement of the gear-like MOFbot may activate these mechanosensitive ion channels, ultimately regulating the permeability of the cell membrane and facilitating transmembrane drug delivery.

Discussion

We have developed a magnetically driven gear-like MOFbot capable of achieving controlled cellular mechanical regulation via magnetic torque-mediated interactions with cellular microvilli. The gear-like MOFbot was successfully fabricated through an epitaxial growth strategy of heterostructural MOFs. The application of an external rotating magnetic field enabled the gear-like MOFbot to perform highly directional and controllable locomotion, including the ability to traverse obstacles. When exposed to an external magnetic field, the gear-like MOFbots interacted with the intricate, intertwined structures of cellular microvilli, inducing mechanical forces. These interactions were quantitatively characterized using FRET and TFM techniques. We systematically demonstrated the capability of gear-like MOFbots to precisely target a single cell and actively permeabilize their membranes. This capability facilitated spatiotemporally regulated calcium signaling and the subcellularly precise delivery of cell-impermeant molecules. Notably, the interaction between MOFbots and cellular microvilli generated controlled mechanical forces, which significantly enhanced intracellular drug delivery efficiency. These findings highlight a micro/nano-robotic system based artificial tool for mechanical force-mediated therapeutic strategies, offering insights for targeted and precision medicine. Beyond HeLa cells, the gear-like MOFbot platform is broadly relevant to diseases where microvilli are central to pathophysiology. In microvillus inclusion disease, defective or absent microvilli disrupt nutrient absorption, while in cancer metastasis, microvilli remodeling influences tumor cell adhesion, migration, and invasion. Our system could probe these altered mechanotransductive processes or serve as a means to modulate them therapeutically. Extensions to immune cells, where microvilli orchestrate antigen sensing and synapse formation, further highlight the versatility of MOFbot-mediated mechanical regulation. These capabilities position our approach as a powerful tool for studying and potentially intervening in microvilli-associated diseases.

While our findings establish microvilli as a critical force-transducing scaffold essential for the mechanoresponse elicited by MOFbots, we acknowledge the inherent complexity of cell-surface interactions. Our model positions microvilli as the primary physical structure for collecting and focusing mechanical force onto the cell. However, the potential contributory roles of specific cell surface receptors in signal transduction, or initial contact mediated by the glycocalyx, warrant further investigation. Future studies employing microrobots functionalized with specific ligands could directly probe the interplay between mechanical force application and receptor-specific signaling pathways. Similarly, detailed investigations into glycocalyx mechanics and its potential entanglement with microrobots

would provide a more comprehensive understanding of the initial adhesion dynamics. In parallel, combining MOFbot-mediated stimulation with high-resolution force measurement tools such as molecular tension sensors, optical tweezers, or DNA-based force probes could bridge the gap between biologically relevant actuation and precise pico- to nanonewton-scale force quantification. Together, these directions would deepen our mechanistic understanding of how targeted mechanical perturbations are transduced into biochemical signals at the single-cell level, while expanding the biomedical potential of micro/nano-robotic systems.

Our results demonstrate the potential of MOFbots for precise mechanostimulation in controlled settings, yet several key challenges must be addressed before their translation to in vivo applications. The dynamic and complex hydrodynamic environment of the circulatory system, for instance, imposes substantial shear stresses that may compromise stable contact between MOFbots and target cells. Furthermore, upon introduction into biological fluids, MOFbots are susceptible to opsonization and rapid clearance by the mononuclear phagocyte system, which would significantly limit their bioavailability and accumulation at desired sites. To overcome these barriers, future designs could incorporate shape optimization to improve flow characteristics and surface modifications—such as PEGylation—to reduce protein adsorption and immune recognition. In parallel, advanced real-time imaging and navigation technologies will be essential for guiding MOFbots in vivo with high spatiotemporal precision. Notably, micro-robotic platforms need not operate independently of molecular targeting paradigms. By conjugating magnetic MOFbots with specific targeting ligands (e.g., antibodies, peptides), it becomes possible to synergize externally controlled navigation with intrinsic biochemical recognition, thereby merging spatial programmability with biochemical specificity. Such a hybrid strategy, rather than replacing conventional targeting, extends the therapeutic toolkit and may substantially improve localization efficiency under physiological flow conditions. Finally, thorough evaluation of safety, biocompatibility, and therapeutic efficacy in physiologically relevant animal models will be crucial. Despite these challenges, the unique capacity of MOFbots to deliver localized mechanical cues in situ offers a promising avenue for mechanobiology research and targeted mechanotherapy.

Methods

Materials and characterization

Titanium isopropoxide (TPOT, 97.0%), aminoterephthalate (99%), zinc nitrate hexahydrate ($Zn(NO_3)_2.6H_2O$, 99.0%), 2-methy-limidazole (HmIm, 98%), methanol (MeOH, 99.5%), N,N-dimethylformamide (DMF, 99.9%), acrylamide, bis-acrylamide, ammonium persulfate (APS), tetramethylethylenediamine (TEMED), phalloidin-TRITC, lipo8000 transfection reagent, plasmid, propidium iodide (PI), rabbit monoclonal anti-phospho-FAK (Tyr397), goat anti-rabbit Alexa Fluor 488 were purchased commercially and used as-received. HeLa cells (Lot: BNCC342189) were purchased from BeNa Culture Collection, China. Scan electron microscope (SEM) images and energy dispersive X-ray (EDX) spectroscopy were captured by Carl Zeiss Microscopy GmbH Gemini SEM 300 and Oxford instruments X-Max, respectively. Powder X-ray diffraction (XRD) patterns were characterized by Rigaku D/max-2500PC diffractometer (Tokyo) at 40 kV, 200 mA. Nitrogen adsorption studies were performed with Micromeritics ASAP 2020 HD88 at 77 K up to 1 bar. Prior to sorption measurements, samples were activated under vacuum at 100 °C for 12 h. FT-IR spectra was analyzed by a Fourier-transformed infrared spectrometer (Nicolet380, Thermo). An electron beam (e-beam) evaporation system (Beijing Technol Science Co.,Ltd.;TEMD500) was used to coat a layer of material (Au, Ni) on the surface of the MIL-125@ZIF-8. Optical videos were taken by a Leica inverted optical microscope (Leica DMi8) with a 40× air objective. Fluorescence images of HeLa cells were taken by confocal laser scanning microscope (CLSM, NiKon A1).

Preparation of experimental device

As shown in Fig. 2a, the reservoir was placed at the center of a home-made triaxial Helmholtz coil, which can create a rotating magnetic field. The sine-wave current was generated using an adjustable function generator and signal amplifier, then input into orthogonally arranged Helmholtz coils to produce a uniform rotating magnetic field in any desired direction. The iron core surrounding by coil enhanced the strength of the generated magnetic field. In addition, the direction of rotation axis, rotational frequency and field strength can be regulated. The coil system was installed on Leica optical inverted microscope equipped with a 40× objective lens.

Synthesis of NH_2-MIL-125

TPOT (0.6 mL) and aminoterephthalate were dissolved in a mixture of DMF (36 mL) and CH_3OH (4 mL). After stirring for 5 min, the mixture was transferred to 100 mL Teflon-line autoclave and heated at 150 °C for 24 h. The obtained yellow solid was isolated by centrifugation, washed for three times with a mixture DMF and CH_3OH at the volume ratio of 9:1 and finally dispersed in methanol (30 mL) to make a stock solution for further use.

Synthesis of gear-like NH_2-MIL-125@ZIF-8 particles

0.4 mL of stock solution containing NH_2-MIL-125 was added into 6 mL 2-Methylimidazole (25 mM) and 10 mL $Zn(NO_3)_2.6H_2O$ (25 mM). The mixture was allowed to react for 4 h at room temperature. The product was collected by centrifugation and washed for three times with methanol.

Synthesis of magnetic gear-like NH_2-MIL-125@ZIF-8 MOFbots

The previously prepared NH_2-MIL-125@ZIF-8 particles were suspended in methanol. Then, 80 μL of methanol suspension containing NH_2-MIL-125@ZIF-8 particles were dropped onto the glass slide (Φ = 40 mm) which was cleaned by sonication and treated with oxygen plasma for 5 min. A layer of 10 nm Ni and 10 nm Au were then sequentially sputtered onto the NH_2-MIL-125@ZIF-8 microparticles using an electron beam (e-beam) evaporation system. The formed NH_2-MIL-125@ZIF-8@Ni@Au MOFbots were collected by sonication in deionized water and centrifugation.

Magnetic actuation and motion analysis

The magnetic actuation system used for driving the gear-like MOFbots comprises five electromagnetic coils, each with 600 turns of 0.4 mm diameter wire and an 8 mm diameter ferrite core to enhance magnetic field strength. A programmable power supply controlled by a myRIO embedded system was employed to generate the coil input signals, allowing flexible and reproducible application of magnetic fields during experiments. The solution containing the magnetic gear-like MOFbots was dropped into the glass slide which was placed in the center of electromagnetic coil pairs (magnetic strength: 6 mT). Horizontal and vertical rotating magnetic fields with different frequency (1 Hz–9 Hz) were employed to power the magnetic gear-like MOFbots. The movements of the gear-like MOFbots were recorded by a charge coupled device (CCD) camera at the frame rate of 20 fps and analysed via python script.

Interaction of magnetic gear-like MOFbots with HeLa cells

The HeLa cells were cultured with DMEM containing 10% FBS and 1% antibiotics. Then, HeLa cells (~5×10^5 cells mL^{-1}) were seed on a glass substrate which can be mounted in the center of magnetic field. 10 μL of magnetic gear-like MOFbots were added to the glass substrate and manipulated on the surface of HeLa cell under rotating magnetic field. The movement of the magnetic gear-like MOFbots on the surface of HeLa cells and the permeability change of the cell membrane were observed using Leica optical inverted microscope equipped with a 40× objective lens.

Cells staining
After 20 min of exposure to the magnetic field, HeLa cells were fixed in 4% paraformaldehyde for 15 min and washed three times with PBS. Thereafter, phalloidin-TRITC (5×10^{-6} M) solution were used to stain the microvilli of HeLa cells for 45 min. Finally, the cells were washed three times and observed through confocal laser scanning microscopy (CLSM).

SEM observation of the cells
HeLa cells were grown on a glass substrate and interacted with the magnetic gear-like MOFbots in a rotating magnetic field for 20 min. Then, HeLa cells were fixed in 4% paraformaldehyde for 15 min and washed three times with PBS. The cells were sequentially dehydrated in ethanol solutions at concentrations of 30%, 50%, 70%, 80%, and 90% for 15 min each, followed by a 30 min dehydration in 100% ethanol. Afterward, the cells were dried using Leica EM CPD300 automated critical point dryer, coated with Au for SEM observation.

Preparation of hydrogels conjugated with fluorescent beads
To measure weak traction forces more accurately, traction force microscopy method based on lastic polyacrylamide-bis-acrylamide (PA) hydrogels containing fluorescent beads were employed. 5 μL red fluorescent carboxylate-modified 200 nm beads (10 mg/mL) were suspended in the 500 μL polyacrylamide mixture containing 7.85% (w/v) acrylamide and 0.27% (w/v) bis-acrylamide, followed by the addition of APS and TEMED. Immediately. 10 μL of the hydrogel solution was placed onto the surface-treated confocal dish and cover it with a coverslip. After 30 min, polymerised gels were stuck at the bottom of confocal dish. The gel surface was activated with 0.5 mg/mL sulfo-SANPAH and then coated with 50 μg/mL collagen I.

Measurement of traction force
HeLa cells were seed onto the hydrogels at a density ~5×10^3 cells/mL and incubated for 24 h. The images of cells and fluorescent beads underneath cell colonies were obtained. Subsequently, the magnetic gear-like MOFbots were added into the cells to interact with them under a magnetic field. The image of fluorescent beads underneath cell colonies treated by rotating magnetic field was obtained. 50 μL of pre-warmed (37 °C) 10% SDS (in PBS solution) was added to lyse the cells completely and the beads were photographed as initial position for result analysis after cell detachment. For the traction force experiments, all of the data were acquired at 40× magnification. Sample drift was corrected by tracking the displacement of fluorescent beads located at the edges away from cells, and the displacement field exerted by cells on the gel was measured by analyzing the positions of the fluorescent beads before and after cell detachment. Based on the pre-measured substrate displacement field and the Young's modulus (18.5 kPa) of the substrate, we reconstructed the cellular traction stress field in ImageJ v1.53.

Plasmid transfection
HeLa cells were spread on the confocal dish at a density of ~5×10^5 cells/mL and were allowed to grow for 12 h. To express β-actin-CFP/YFP-β-actin fusion proteins, the Lipo8000 Transfection Reagent (Beyotime Biotechnology, China) was employed to introduce the plasmid of Actin-cpstFRET-Actin (Addgene plasmid # 80643) into the cells. After a successful transfection, the magnetic gear-like MOFbots were added into the cells. Under a horizontal rotating magnetic field (7 Hz), the dynamic changes in FRET signals were observed. To assess potential baseline fluctuations in intracellular FRET signals, HeLa cells expressing actin-based force probes were subjected to the same experimental conditions as the MOFbots stimulation assays, except that no magnetic field was applied.

To explore the changes in Ca^{2+} concentration in HeLa cell, the plasmid of pCMV-jGCaMP7s (Beyotime Biotechnology, China) were transfected using the same protocol described above.

Ezrin-siRNA transfection
HeLa cells were cultured in DMEM medium containing 20% FBS and then transfected with 50 nM ezrin small interfering RNA (siRNA) using Lipo8000 Transfection Reagent (Beyotime Biotechnology, China) for 48 h. The designed ezrin-targeting siRNA sequences are TCAGGAACATCTCTTTCAA, GGACTATGAGGAGAAGACA, CTGCGGAGCTTGCAGAATA.

Inhibition of mechanosensitive ion channels
HeLa cells transfected with plasmid of pCMV-jGCaMP7s were pre-treated with specific pharmacological inhibitors. For PIEZO1 inhibition, cells were incubated with 1 μM GsMTx4 (MedChemExpress, USA), a peptide toxin derived from the Chilean rose tarantula (*Grammostola spatulata*) that selectively blocks PIEZO channels. For TRPV4 inhibition, cells were treated with 1 μM HC-067047 (MedChemExpress, USA), a selective TRPV4 antagonist. Inhibitors were added to the culture medium 30 min prior to MOFbots stimulation and maintained throughout the imaging process. Following inhibitor treatment, calcium dynamics were monitored and fluorescence changes were recorded under magnetic field.

Immunofluorescence staining
HeLa cells were fixed in 4% paraformaldehyde for 15 min and washed three times with PBS. Subsequently, the cells were permeabilized using 0.25% v/v PBST (Triton-X 100 in PBS) for 10 min. To avoid nonspecific protein adsorption, the samples were incubated for 1 h in a blocking solution containing 1% (w/v) bovine serum albumin (BSA) in PBST (0.1% v/v). Next, samples were incubated overnight at 4 °C with primary antibodies against phospho-FAK (Tyr397) (1:300, 44-624 G, Thermo Scientific), Piezo1 (1:200, 28511-1-AP, Proteintech), TRPV4 (1:200, ACC-124-25 UL, Thermo Scientific). After incubating with the primary antibody, the samples were washed twice with PBST and three times with PBS. Subsequently, the samples were then incubated at room temperature with goat anti-rabbit Alexa Fluor 488 (Thermo Scientific, 1:500 dilution) and DAPI for 60 min, after which they were washed twice with PBST and three times with PBS. Immunofluorescence images were examined by confocal laser scanning microscope (CLSM, NiKon A1).

Transmembrane transportation of PI
HeLa cells were cultured on a glass substrate. The glass slide was positioned at the center of a magnetic field (7 Hz, 6 mT) and placed on the platform of an inverted optical microscope. 10 μL of magnetic gear-like MOFbots adsorbed with PI were added to the cells and guided toward the target cell and altered their cell membrane permeability. The motion of the magnetic gear-like MOFbots and the entry of PI into the cell were observed using fluorescence microscopy. In addition, the fluorescence intensity of PI within the cells was measured by flow cytometry using FlowJo v10 software.

CCK-8 assay
HeLa cells were seeded at a density of 5×10^3 cells per well in 96-well plates and cultured in a 5% CO_2 atmosphere at 37 °C for 24 h. Various concentrations of magnetic gear-like MOFbots adsorbed with PI and DOX were separately introduced into the culture medium. After a duration of 10 min in the rotating magnetic field (7 Hz, 6 mT), the medium was removed and the cells were washed with PBS. Following this, CCK-8-containing medium was added to each well, and the cells were incubated for another 1 h. The absorbance at 450 nm was then measured using a microplate reader.

Reporting summary
Further information on research design is available in the Nature Portfolio Reporting Summary linked to this article.

Data availability

The data generated or analysed during this study are included in this published article/Supplementary Information/Source Data file. Source data is available for Figs.1d–g, 2c, 2d, 2f, 2i, 2k, 3e–g, 4c, 4d, 4h, 4i, 5c–f, 5h, 6d, 6f–h and Supplementary Figs. 3, 4, 6, 8, 10b, 12b, 12c, 13b, 13c, 15b, 19c, 20b, 21, 22a, 22b, 24 in the associated source data file. The raw data generated in this study have also been deposited in the Zenodo database under accession code [10.5281/zenodo.18495219]. Source data are provided with this paper.

Code availability

Code associated with our paper is available at https://github.com/alfredyang93/Demo-datasets.

References

1. Zhang, Y. & Habibovic, P. Delivering mechanical stimulation to cells: state of the art in materials and devices design. *Adv. Mater.* **34**, e2110267 (2022).
2. Humphrey, J. D., Dufresne, E. R. & Schwartz, M. A. Mechanotransduction and extracellular matrix homeostasis. *Nat. Rev. Mol. Cell Biol.* **15**, 802–812 (2014).
3. Lin, Y. C. et al. Force-induced conformational changes in PIEZO1. *Nature* **573**, 230 (2019).
4. Savadipour, A. et al. Membrane stretch as the mechanism of activation of PIEZO1 ion channels in chondrocytes. *Proc. Natl. Acad. Sci. Usa.* **120**, e2221958120 (2023).
5. Andreu, I. et al. The force loading rate drives cell mechanosensing through both reinforcement and cytoskeletal softening. *Nat. Commun.* **12**, 4229 (2021).
6. Dasgupta, I. & McCollum, D. Control of cellular responses to mechanical cues through YAP/TAZ regulation. *J. Biol. Chem.* **294**, 17693–17706 (2019).
7. Elosegui-Artola, A. et al. Force triggers YAP nuclear entry by regulating transport across nuclear pores. *Cell* **171**, 1397 (2017).
8. Korkmazhan, E. & Dunn, A. R. The membrane-actin linker ezrin acts as a sliding anchor. *Sci. Adv.* **8**, eabo2779 (2022).
9. Du, Z. et al. Mechanosensory function of microvilli of the kidney proximal tubule. *Proc. Natl. Acad. Sci. Usa.* **101**, 13068–13073 (2004).
10. Cai, E. et al. Visualizing dynamic microvillar search and stabilization during ligand detection by T cells. *Science* **356**, eaal3118 (2017).
11. Weinbaum, S., Guo, P. & You, L. D. A new view of mechanotransduction and strain amplification in cells with microvilli and cell processes. *Biorheology* **38**, 119–142 (2001).
12. Iyer, S., Gaikwad, R. M., Subba-Rao, V., Woodworth, C. D. & Sokolov, I. Atomic force microscopy detects differences in the surface brush of normal and cancerous cells. *Nat. Nanotechnol.* **4**, 389–393 (2009).
13. Schneeberger, K. et al. An inducible mouse model for microvillus inclusion disease reveals a role for myosin Vb in apical and basolateral trafficking. *Proc. Natl. Acad. Sci. USA.* **112**, 12408–12413 (2015).
14. Delon, L. C. et al. A systematic investigation of the effect of the fluid shear stress on Caco-2 cells towards the optimization of epithelial organ-on-chip models. *Biomaterials* **225**, 119521 (2019).
15. Miura, S., Sato, K., Kato-Negishi, M., Teshima, T. & Takeuchi, S. Fluid shear triggers microvilli formation via mechanosensitive activation of TRPV6. *Nat. Commun.* **6**, 8871 (2015).
16. Aramesh, M. et al. Nanoconfinement of microvilli alters gene expression and boosts T cell activation. *Proc. Natl. Acad. Sci. USA.* **118**, e2107535118 (2021).
17. Luo, M., Feng, Y., Wang, T. & Guan, J. Micro-/nanorobots at work in active drug delivery. *Adv. Funct. Mater.* **28**, 1706100 (2018).
18. Li, J. X., De Avila, B. E. F., Gao, W., Zhang, L. F. & Wang, J. Micro/nanorobots for biomedicine: delivery, surgery, sensing, and detoxification. *Sci. Robot.* **2**, eaam6431 (2017).
19. Gultepe, E. et al. Biopsy with thermally-responsive untethered microtools. *Adv. Mater.* **25**, 514–519 (2013).
20. Wu, Z. et al. A swarm of slippery micropropellers penetrates the vitreous body of the eye. *Sci. Adv.* **4**, eaat4388 (2018).
21. Gao, Y. et al. Magnetically manipulated optoelectronic hybrid microrobots for optically targeted non-genetic neuromodulation. *Adv. Mater.* **36**, 2305632 (2024).
22. Lin, Z. et al. Magnetically actuated peanut colloid motors for cell manipulation and patterning. *ACS Nano* **12**, 2539–2545 (2018).
23. Chen, W. J. et al. Recent progress of micro/nanorobots for cell delivery and manipulation. *Adv. Funct. Mater.* **32**, 2110625 (2022).
24. Gao, Y. X. et al. Template-guided silicon micromotor assembly for enhanced cell manipulation. *Angew. Chem.* **63**, e202405895 (2024).
25. Zhou, H. J., Mayorga-Martinez, C. C., Pané, S., Zhang, L. & Pumera, M. Magnetically driven micro and nanorobots. *Chem. Rev.* **121**, 4999–5041 (2021).
26. Cao, Y. et al. Magnetic continuum robot with modular axial magnetization: design, modeling, optimization, and control. *IEEE Trans. Rob.* **41**, 1513–1532 (2025).
27. Liu, C. et al. Site-specific growth of MOF-on-MOF heterostructures with controllable nano-architectures: beyond the combination of MOF analogues. *Chem. Sci.* **11**, 3680–3686 (2020).
28. Bergert, M. et al. Confocal reference free traction force microscopy. *Nat. Commun.* **7**, 12814 (2016).
29. Guo, J., Wang, Y., Sachs, F. & Meng, F. Actin stress in cell reprogramming. *Proc. Natl. Acad. Sci. Usa.* **111**, E5252–E5261 (2014).
30. Yang, J. et al. Photo-tunable hydrogels reveal cellular sensing of rapid rigidity changes through the accumulation of mechanical signaling molecules. *Cell Stem Cell* **32**, 121–136 (2025).
31. Zhang, M. et al. Cell mechanical responses to subcellular perturbations generated by ultrasound and targeted microbubbles. *Acta Biomater.* **155**, 471–481 (2023).
32. Yuan, F., Yang, C. & Zhong, P. Cell membrane deformation and bioeffects produced by tandem bubble-induced jetting flow. *Proc. Natl. Acad. Sci. USA.* **112**, E7039–E7047 (2015).
33. Yang, T. et al. Microwheels on microroads: enhanced translation on topographic surfaces. *Sci. Robot.* **4**, eaaw9525 (2019).
34. Chien, S. Molecular and mechanical bases of focal lipid accumulation in arterial wall. *Prog. Biophys. Mol. Biol.* **83**, 131–151 (2003).
35. Shi, Z., Graber, Z. T., Baumgart, T., Stone, H. A. & Cohen, A. E. Cell membranes resist flow. *Cell* **175**, 1769–1779 (2018).
36. Katta, S., Krieg, M. & Goodman, M. B. Feeling force: physical and physiological principles enabling sensory mechanotransduction. *Annu. Rev. Cell Dev. Biol.* **31**, 347–371 (2015).

Acknowledgements

This work was supported by Shenzhen Science and Technology Program (RCJC20231211090000001 to X.M.), Shenzhen Medical Research Fund (A2403068 to D.J.), Shenzhen Science and Technology Program (GXWD20231129101105001 to X.M., KJZD20231023100302006 to D.J.), National Natural Science Foundation of China (52472280 to D.J., 82402730 to Y.W.), Macau Foundation for Development of Sicence and Technology (0008/2024/RIA1 to X.M.), China Postdoctoral Science Foundation (2024M763882 to X.L.).

Author contributions

X.L. synthesized and characterized the MOFbots, analyzed the interaction between MOFbots and cellular microvilli, and wrote the paper. Y.W. was responsible for video recording of the MOFbots and data analysis. L.L. simulated the flow field around the MOFbots. N.L. simulated the interaction between the gear-like MOFbot and cellular microvilli. Z.Y. analyzed the distribution of gear-like MOFbots within cellular microvilli using the Unet++ network model. P.W. analyzed the cell substrate deformation induced by the MOFbot. X.Y. and J.G. revised the

manuscript. Y.W., D.J. and X.M. conceived the initial idea, supervised the project, and edited the paper.

Competing interests
The authors declare no competing interests.

Additional information
Supplementary information The online version contains supplementary material available at https://doi.org/10.1038/s41467-026-70052-8.

Correspondence and requests for materials should be addressed to Yong Wang, Dongdong Jin or Xing Ma.

Peer review information *Nature Communications* thanks Pierre Bongrand and Jianguo Guan for their contribution to the peer review of this work. [A peer review file is available].